MEDWIN PUBLISHERS
Committed to Create Value for Researchers

Petroleum & Petrochemical Engineering Journal
ISSN: 2578-4846

Inventive Visible-Light 2D/2D GC_3N_4/PVA@Biocl Photocatalyst for Improving Decontamination of Hazardous Dye from Wastewater: Modeling and Optimization

Motawea EA*

Department of Analysis and Evaluation, Egyptian Petroleum Research Institute (EPRI), Egypt

***Corresponding author:** Eman A Motawea, Analysis and Evaluation Department, Egyptian Petroleum Research Institute (EPRI), 1 Ahmed El Zomor St. Nasr City, Cairo, 11727, Egypt, Email: eman.chemie@gmail.com

Research Article

Volume 8 Issue 4

Received Date: November 03, 2024

Published Date: December 31, 2024

DOI: 10.23880/ppej-16000402

Abstract

In this study, an efficient nanocomposite gC_3N_4/PVA@BiOCl was synthesized hydrothermally using environmentally sustainable polyvinyl alcohol polymer and gC_3N_4 decorated by BiOCl. All chemical, structural, morphological, and photocatalytic features were examined, by examining the band structures of the catalyst's components, it is achievable to effectively create a unique Z-scheme heterojunction, which produces additional active sites and speeds up the process of separating the photo-generated species in addition to improving the light absorption efficiency. Their utility to eliminate a positively charged dyestuff, basic blue (BB) furthermore a negatively charged dyestuff, orange G (OG) was investigated. In contrast to single-phases BiOCl or gC_3N_4, the results showed that the gC_3N_4/PVA@BiOCl photocatalyst showed more degrading activity for BB and OG. The gC_3N_4/PVA@BiOCl exhibited a maximum photocatalytic activity of 92.7% toward the remediation of orange G while degrading BB dye with 81.9% within 300 min. The response surface methodology (RSM) was utilized to statistically assess the influences of initial dye concentration and the photocatalyst dose on the degradation performance. Under optimum conditions of photocatalyst dose 0.85g/L, initial dye concentration of 10 ppm the degradation reached 100% and 98% for OG and BB dye respectively. The radical trapping studies confirmed that $\bullet O^{2}$- radicals and h+ are the primary active forms of gC_3N_4/PVA@BiOCl during photocatalysis. gC_3N_4/PVA@BiOCl composite retained more than 93% of its initial degradation efficiency in the subsequent photocatalytic degradation of OG dye even after the fourth cycle.

Graphical Abstract:

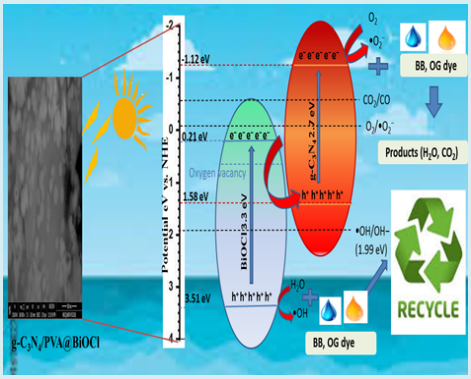

Keywords: GC_3N_4/PVA@Biocl Nanocomposite; Z-Scheme Heterojunction; Visible Light Photodegradation; Basic Blue and Orange G Dye; Response Surface Methodology

Abbreviations

BB: Basic Blue; OVs: Oxygen Vacancies; RSM: Response Surface Methodology; CCD: Xentral Composite Design; XRD: X-Ray Diffraction Patterns; DRS: Diffuse Reflectance Spectroscopy; PL: Photoluminescence; ANOVA: Analysis of Variance; DF: Degrees of Freedom; MS: Mean Squares; SS: Sum of Squares; PBQ: P-Benzoquinone; EDTA: Ethylene Diamine Tetraacetic Acid Disodium Salt.

Introduction

Energies problems & destruction of the environment are major worldwide challenges that have attracted an excess of consideration in recent generations. The quality of human drinking water is seriously affected by water contamination. Various contaminants, including dyes (basic blue BB, and orange G OG), antibiotics, petrochemicals, pesticides, industrial wastes, and more, are discharged in both direct and indirect ways into aquatic streams generating significant pollution to the environment [1,2]. It should be vitally important to destroy these pollutants using an ecological strategy to ensure the peaceful growth of humanity. To date, numerous methods being created to remove toxicity of the harmful contaminants and provide a safe environs for people to live in Li, et al. [3]. Among these tactics, photocatalytic technology has come to light with the advantages of being an efficient use of solar energy, environmentally friendly, reasonably priced, and highly effective at degrading organic pollutants. As a result, it has developed quickly in different areas [4]. In many cases, semiconductor photocatalysts have been utilized as an essential component to carry out photocatalysis effectively. Two important variables that affect photocatalytic efficacy are semiconductor bandgap and the separation and convey characteristics of holes produced by light (h+) and electrons (e-). It is generally true that the photocatalytic system's presence of h^+, $\cdot O^-_2$, and ·OH will accelerate the decontamination of toxic pollutants. The photocatalytic components must have an excellent separation of photoinduced e^-/h^+ to produce significant quantities of ·OH and ·O-2. A photocatalytic reaction can only be generated once the generated e-/h^+ pairs reach on outermost layer of the photocatalytic substances. Research has shown that the semiconductor catalyst's crystalline component, particle diameter, shape, exposed crystalline surface, crystal imperfections, and capturing conditions all have an impact on the carriers' ability to separate. Because the photocatalyst largely controls the photocatalytic performance, it is vital to regulate all these conditions in the semiconductor [1,5,6]. There is a growing interest in Bi-based photocatalytic compounds because of their unique physical characteristics, including ferroelectricity, optical effect, and photocatalytic qualities, which are related to its structure of two $6S^2$ lone electron pairs and the steric hindrance of Bi^{3+} [7]. BiOCl has garnered significant interest across several Bi-based photocatalytic compounds due to its noteworthy characteristics. BiOCl is renowned for having a distinct electrical structure, layered crystal structure, and exceptional heat stability [8]. According to the mathematical computation, the conduction band of BiOCl is related to the Bi 6p orbital, while the valence band owing to the O 2p and Cl 2p orbits. When exposed to illumination, e- will move out of the Cl 2p orbital to the Bi 6p orbital, producing pairs of photogenerated e^- and h^+. BiOCl is a UV light-responsive material that has an indirect bandgap (Eg) of 3.2 eV, making it an indirect semiconductor. However, the utilization of BiOCl is severely limited by its short carrier lifespan and poor visible light usage efficiency [9-12]. Frequent point defects or bulk defects on the catalyst are known as vacancies, and they typically contain anion vacancies (like O, S, N, etc.) and cation vacancies (like Bi, Zn, Ti, etc.) [13-15]. among the largest and most prevalent defects in oxide semiconductor photocatalytic materials are Oxygen Vacancies (OVs) [16,17], which can have a significant impact on the material's surface adsorption, electrical structure, and light absorption. Prior investigation has verified that the existence of oxygen vacancies lowers the material's Eg and increases its light absorption [18-21].

By acting as the separation center for e^-/h^+ pairings, an adequate number of OVs can aid in carrier separation and enhance the photocatalytic function. Moreover, O2 adsorbed on OVs can be activated by OVs, forming $\cdot O^-_2$ with the photoexcited electrons. Furthermore, the addition of OVs causes the photocatalysts' Fermi level to rise, and the defect level manifests itself close to the CB [22-27]. Many techniques have been devised to build OVs [14,28-30]. Among the compounds that compose polyhydroxy polymers is polyvinyl alcohol (PVA). Its ability to dissolve in water is an enormous benefit, and it can be utilized as a surfactant to change the shape of the photocatalysts and to create a visible light-responsive photocatalyst. PVA is a potentially beneficial component for photocatalyst preparation due to its low cost of manufacturing and simplicity of removal [31]. Thus, it is expected that PVA will influence the crystal formation of BiOCl in solvothermal synthesized structures, causing OVs and increasing photocatalytic activity [32]. Graphitic carbon nitride (g-C_3N_4) has attracted a lot of interest, due to its many notable qualities, including its good thermal and structural stability, minimal toxicities, its appropriate band structure, and its affordability [33-35]. It can be synthesized easily by pyrolyzing organic reactants which include carbon and/or nitrogen. Furthermore, g-C_3N_4 has been used in a variety of contexts, particularly in the photodegradation of various

organic pollutants. g-C_3N_4 exhibits encouraging visible light-sensitive photoactivity with a narrow bandgap of 2.7 eV [36,37]. fortunately, the inadequate separation efficiency of photo-induced electron-hole pairs at the interface limits the use of the single g-C_3N_4 photocatalyst. Various techniques have been explored to alter g-C_3N_4 to enhance photocatalytic activity. In essence, g-C_3N_4 is a great option for creating heterojunction photocatalysts with other semiconductors because it has a rich surface area and an energy band position that is negative compared to most semiconductors [36-38]. In this instance, g-C_3N_4 and PVA will be added to the solvothermal synthetic system of BiOCl to create g-C_3N_4/PVA@BiOCl photocatalysts with rich OVs. e^-/h^+ pairs will be enhanced by controlling the morphology of BiOCl and creating rich OVs using a simple and moderate solvothermal synthesis method.

As a result, the generated g-C_3N_4/PVA@BiOCl will have higher catalytic activity than the blank g-C_3N_4 and BiOCl for the degradation of basic blue (BB) and, orange G (OG) dyes. This work could offer fresh perspectives on the development of broad bandgap visible-light-driven photocatalysts in the future. Herein, response surface methodology (RSM) coupled with central composite design (CCD) was employed for establishing a link between response (dye degradation %) as well as degradation factors (pH, initial dye concentration, and photo-catalyst dosage), investigating the relationship among independent factors as well as process optimization.

Experimental

Chemicals

Chemicals used in this study were ultra-pure, also deionized water was employed for all experiments. Bismuth nitrate pentahydrate $(BiNO_3)_3.5H_2O$, urea, and Polyvinyl alcohol (PVA) were acquired by Sigma Aldrich. Potassium chloride (KCl), Basic blue (BB), and Orange G (OG) were purchased from Alfa Aesar.

Preparation of g-C_3N_4 Nanosheets

Urea was used as the raw component for the synthesis of g-C_3N_4, and 5gm of urea powder was heated at 500 °C with an Ar gas flow. Next, at 90°C, 3 g of powdered g-C_3N_4 was incorporated with 1 M of HNO_3 and stirred for 6 hours. Following centrifugation of the suspension, the precipitate was twice washed with ultrapure water and vacuum-dried for 24 hours at 70°C [39].

Preparation of Biocl and G-C_3N_4/PVA@Biocl Samples

40 milliliters of vinegar acid and twenty milliliters of double distilled water were used to dissolve 5g of $Bi(NO_3)_3.5H_2O$ and 0.7679 g of KCl, respectively. To the KCl aqueous solution, PVA with a weight ratio of 4% (PVA/$Bi(NO_3)_3.5H_2O$) was added and heated till the amount of PVA was dissolved. Conversely, g-C_3N_4 was dispersed at a weight ratio of 50% (g-C_3N_4/ $Bi(NO_3)_3.5H_2O$) into a glacial acetic acid solution before the addition of $Bi(NO_3)_3.5H_2O$. After vigorously stirring the g-C_3N_4/$Bi(NO_3)_3.5H_2O$-vinger acid solution, the KCl-PVA aqueous solution was gradually dripped into it, creating a white precipitate. The precipitate was then moved to an autoclave then heated to 180°C for 24 hours. g-C_3N_4/PVA@BiOCl were obtained following filtering, rinsing, along with drying at 70°C for 12 hours [1]. The pristine BiOCl was prepared with the same procedure without the addition of g-C_3N_4 and PVA. A schematic illustration of the g-C_3N_4/PVA@BiOCl synthesis procedure is provided in Figure 1.

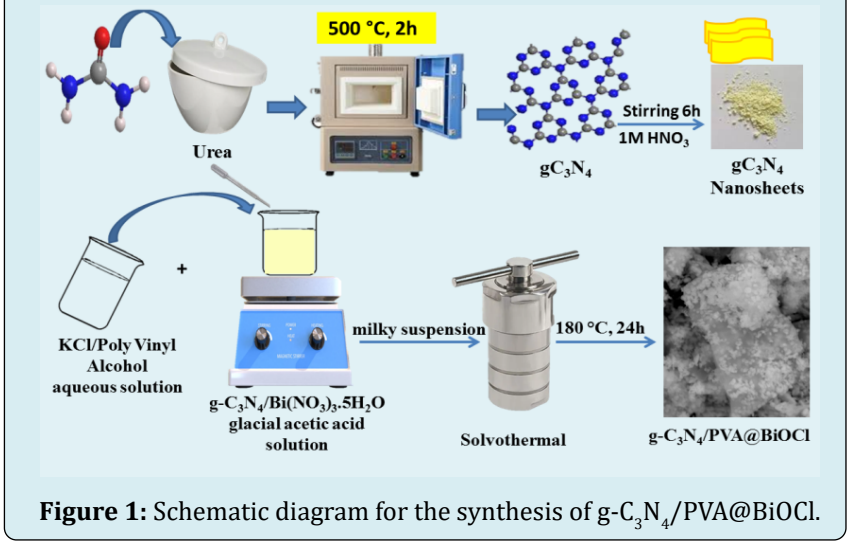

Figure 1: Schematic diagram for the synthesis of g-C_3N_4/PVA@BiOCl.

Characterization

The IR spectra of synthesized hydrogels have been captured using FT-IR spectroscopy (Shimadzu FTIR-4200) spectrometer. X-ray Diffraction patterns (XRD) of the samples were obtained utilizing a contemporary PAN analytical diffractometer, Xpert PRO type. The prepared catalysts were measured throughout the diffraction angle (2θ) range of 5° and 80°. The surface features of the catalysts were investigated on an HR-SEM (JEOL, JSM model no: 6360). investigation of scanning electron microscopy with energy dispersive X-ray (SEM-EDX) has been accomplished by utilizing scanning electron microscope JEOL GSM 6510LV. The optical characteristics were assessed using UV/Vis diffuse reflectance spectroscopy (DRS) at the wavelength of 200-800 nm (HITACHI-3900) and photoluminescence (PL) spectroscopy (HITACHI F7000). The photoelectrochemical measurements were performed utilizing an OrigaFlex-Pack OGF01A/potentiostat−galvanostat (Origalys, France) system. The surface oxidation states and compositional structure were collected via XPS spectra on K-ALPHA (Thermo Fisher Scientific, USA) with monochromatic X-ray Al K-α radiation of −10−1350 eV and a spot size of 400 μm at a pressure of 10−9 m bar with a full-spectrum pass energy of 200 eV and a narrow-spectrum of 50 eV. A UV/Vis. spectrophotometer (JENWAY-6505) was utilized for the detection of basic blue (BB) and orange G OG dye concentrations at λmax of 655 nm and 490 nm respectively.

Photocatalytic Investigation and Variables Optimization

To assess the photocatalytic implementation for the synthesized photocatalysts (BiOCL, g-C_3N_4, and g-C_3N_4/PVA@BiOCl), BB and OG dye were degraded under visible light illumination with neutral pH values. Halogen lamp (300 W/cm^2) served as an origin of visible light (λ > 420 nm) that was located 25 Cm above a batch system. 0.01 g of each photocatalyst was shaken with 25 mL of BB and OG dye aqueous solution (50 mg/l). The combinations were then allowed to stir for 1h in the darkness until attaining adsorption-desorption balance. Afterward, the mixture was then illuminated with visible light irradiation for 300 min. Treated water was obtained at various times and centrifuged to isolate the photocatalyst from the dye solution after that the absorbance spectra of the dye solution were then investigated utilizing a UV–Vis spectrophotometer.

The following equation was used to determine the percentage degradation of BB and OG dye:

$$\text{Degradation efficiency } \% = \left[\left(C_0 - C_t\right)/C_0\right] \times 100\ \% \quad (1)$$

Where C_0 and C_t refer to the initial concentration of BB and OG dye and the concentration at a specific time after the reaction.

The reaction rate constant was determined with the Langmuir-Hinshelwood kinetic model using the subsequent equation;

$$\ln\left(C_0/C_t\right) = kt \quad (2)$$

While C_0, C_t, K, and t refer to the starting concentration of the dye solution, the concentration of dye after a definite time of the reaction, the reaction rate constant, and the time of the reaction, respectively.

For optimizing the influence of various variables such as catalyst dose (0.25, 0.425, 0.85, 1.27, and 1.75 g/L), and initial dye concentration (10, 50, 100, 150, and 200) on the degradation efficiency of g-C_3N_4/PVA@BiOCl a simplified response surface methodology (RSM) has been included depending on the central composite design (CCD). Each degradation factor has five levels described as +α, +1, 0, −1, and -α. Furthermore, the complaint influence of several factors on the degradation performances of different photocatalysts was subjected to statistical analysis by the analysis of variance (ANOVA). Design- Expert software (V.11) was utilized to perform computational analysis of results. To obtain the absorption equilibrium, every experiment was shaken in the dark for one hour. After that, they were run for three hundred minutes in the presence of visible light. The subsequent second-degree polynomial formula characterized the degrading effectiveness trend of the dye:

$$Y = \beta_0 + \sum_{i=1}^{3} \hat{a}_i X_i \sum_{i=1}^{3} \hat{a}_{ii} X_{ii}^2 + \sum_{i=1}^{3} \sum_{j=1}^{2} \beta_{ij} X_i X_j \quad (3)$$

Where Y is the response variable, β_0, β_i, β_{ij}(ij), and βii are the regression coefficients for intercept, linear effect, double interaction, and quadratic effects, respectively, and X_i and X_j are the independent variable

Results and Discussion

XRD Patterns

Figure 2a displays the crystal structure and phase composition by examining the XRD diffraction patterns of the prepared g-C_3N_4, BiOCl, and g-C_3N_4/PVA@BiOCl. The two primary diffraction peaks of the g-C_3N_4 that appear at 2θ of 13.03° and 27.83°, respectively correlate to the crystalline patterns of (100) and (002), the distinctive diffraction patterns match JCPDS File No. 87–1526 fairly well [40,41]. Diffraction patterns at 2θ of 11.99°, 24.04°, 25.78°, 32.41°, 33.46°, 34.67°, 36.47°, 40.80°, 46.55°, 48.27°, 49.70°, 54.00°, 54.99°, 58.50°, 60.65°, 68.02°, 74.99°, and 77.58° are

displayed in the tetragonal phase BiOCl, these correspond to the reflection from (001), (002), (101), (002), (102), (111), (003), (112), (200), (201), (211), (211), (114), (212), (114), (220), (301), and (310) planes, respectively. The peaks and JCPDS File No. 06-0249 have a good correlation [42,43]. The patterns of the g-C_3N_4/PVA@BiOCl composites Figure 2a showed that all of the diffraction peaks agreed well with the BiOCl tetragonal phase (JCPDS Card No. 06-0249), indicating that the coupled g-C_3N_4 did not affect the BiOCl lattice structure.

Additionally, the diffraction pattern intensity of the (001) crystalline plane of BiOCl seems to decline and moves to a high angle at 2θ of 12.03°, indicating that the crystal spacing gets smaller and causes OVs [1].

However, g-C_3N_4's distinctive peaks were not as visible as those of BiOCl because of their lower intensity and crystallinity [44]. Furthermore, the absence of any discernible impurity phases implies that the BiOCl/g-C_3N_4 heterojunctions in their prepared state were two-phase hybrids.

FT-IR Analysis

Utilizing vibrational spectroscopy FT-IR, the functional group present in the synthesized photocatalysts was examined and depicted in Figure 2b. The spectra of pristine BiOCl showed three prominent adsorption peaks. The stretching vibration forms of exterior hydroxyl groups and acutely absorbed water molecules, respectively, are attributed to the bands at 3435 and 1620 cm^{-1}. Nonetheless, the distinctive symmetrical stretching vibration of the Bi–O chemical bonds in BiOCl was identified with a peak at 530 cm^{-1} [41]. The samples containing g-C_3N_4 displayed a peak at around 3160 cm^{-1}, owing to the vibration of the -NH_2 group. In the same way, the triazine ring's usual vibrational mode was attributed to the pattern rising at 805 cm^{-1}. One possible explanation for the peaks at 1305 and 1230 cm^{-1} could be the aromatic C–N bonds stretching. Furthermore, the C=N stretching could be responsible for the peaks that emerged at 1640 cm^{-1}, 1555 cm^{-1}, and 1416 cm^{-1} [34-36,40]. According to the results, as an interaction between g-C_3N_4 and BiOCl is formed, most of the g-C_3N_4 photocatalyst remains unaffected. Additionally, the spectra of the g-C_3N_4/PVA@BiOCl photocatalyst revealed the peak at 525 cm^{-1}. These are ascribed to the unique symmetrical stretching vibration of the Bi-O bond. Vibrational spectra verify that the heterojunction of g-C_3N_4/PVA@BiOCl was successfully fabricated.

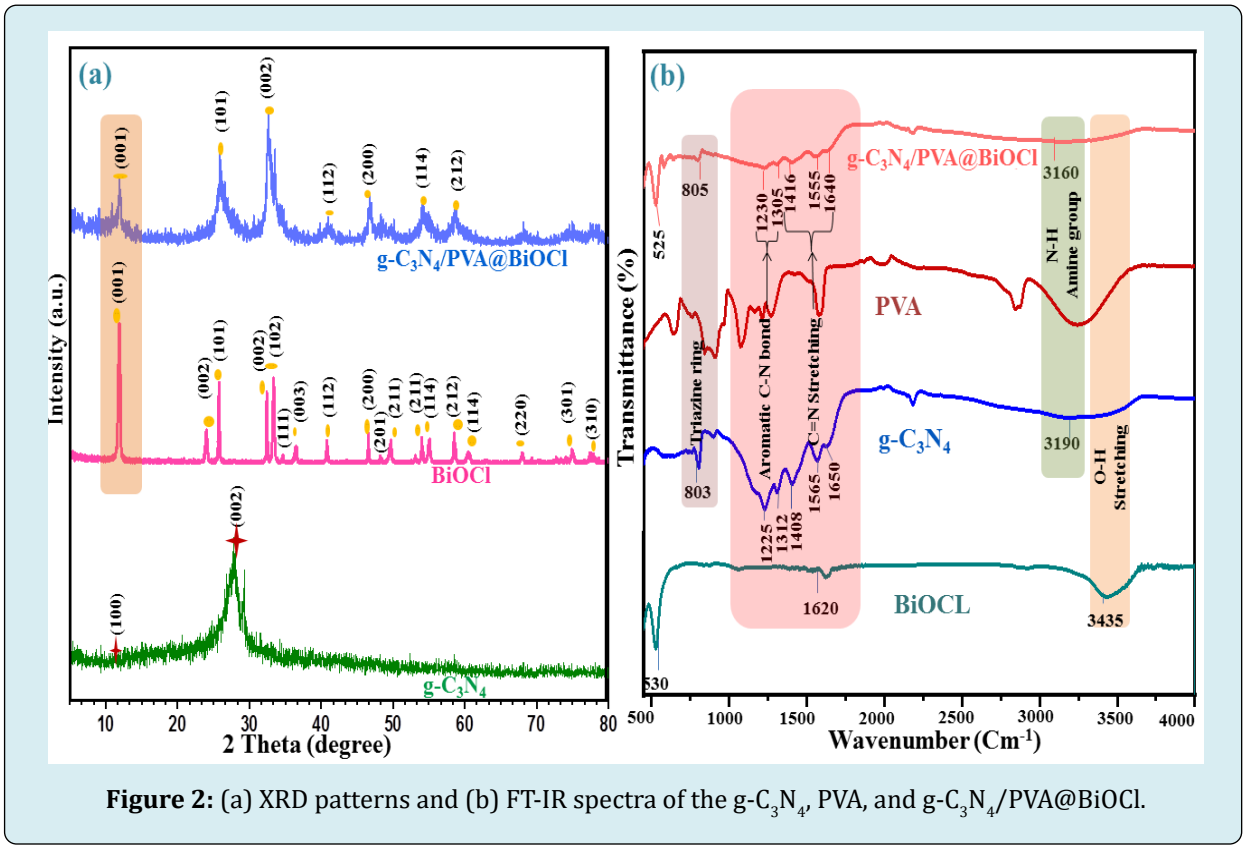

Figure 2: (a) XRD patterns and (b) FT-IR spectra of the g-C_3N_4, PVA, and g-C_3N_4/PVA@BiOCl.

Morphology

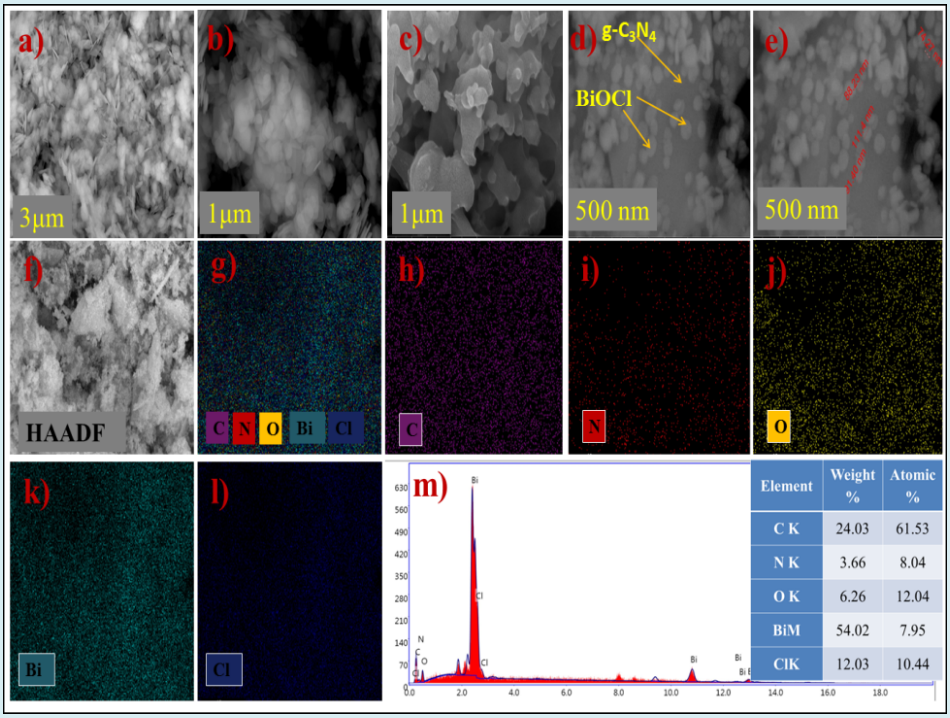

Figure 3: FE-SEM images of (a, b) BiOCl at different magnifications, (c) g-C_3N_4, (d, e) g-C_3N_4/PVA@BiOCl, (f) HAADF photograph of g-C_3N_4/PVA@BiOCl, (g-l) elemental mapping of C, N, O, Bi, and Cl, and (j) EDS spectrum of g-C_3N_4/PVA@BiOCl.

FESEM was accustomed to analyzing the morphological features of the synthesized photocatalysts. As illustrated in Figure 3a, the morphology of BiOCl reveals an incredibly smooth surface and a thick lamellar structure; the thick lamellae are assembled to form a sheet shape in Figure 3b. The results of studies of the UV-Vis diffuse reflectance spectrum attest to the sheet's excellent form for light utilization [40]. The g-C3N4 sample shown in Figure 3c exhibits a typical layer structure, with sheets acting as the fundamental unit that are seen as pliable, loose agglomerates. Furthermore, it was discovered that BiOCl nanosheets are uniformly dispersed across the surface of g-C_3N_4 nanosheets and that the initial shape of g-C_3N_4 was not noticeably altered when BiOCl was synthesized in the presence of g-C_3N_4 nanosheets (Figures 3d & 3e). Additionally, the typical size of BiOCl's lamellar thickness ranged from 74 to 111 nm, resulting in a noticeably thinner 2D/2D sheet structure for g-C_3N_4/PVA@BiOCl nanocomposite [45,46]. The g-C_3N_4/PVA@BiOCl heterojunction's 2D/2D structure has an excellent interface and creates an imposed electric field, that may facilitate the separation of e^- and h^+, also the small size of the sheets form can increase the specific surface area. It is proven that carbon, nitrogen, bismuth, oxygen, and chlorine are equally distributed over the composite nanosheets, as seen in the matching high-angle annular dark-field picture (HAADF) and EDS mapping images (Figures 3f-3l). The weight percentages of the Bi, Cl, C, N, and O elements are 54.02, 12.03, 24.03, 3.66, and 6.26, respectively, according to the result in Figure 3m shows that no contaminants were present during the preparation of the g-C_3N_4/PVA@BiOCl.

XPS Study

X-ray photoelectron spectroscopy (XPS) was applied to examine the elemental constitution and chemical state of the g-C_3N_4/PVA@BiOCl composite. The survey spectrum of g-C_3N_4/PVA@BiOCl in Figure 4a shows that Bi, Cl, C, N, and O elements are present in the photocatalyst. The findings of the elemental mapping study and the EDX analysis in Figure 3 are in good correlation with this, suggesting that the conjugation of g-C_3N_4, and BiOCl was successful. According to Figure 4b, the high-resolution Bi 4f spectra show four peaks assigned as Bi $4f_{7/2}$ and Bi $4f_{5/2}$ at 159.39 eV and 164.37 eV, respectively, that is attributed to Bi^{3+}'s existence [47]. Although the noticed peaks of Bi $4f_{7/2}$ and Bi $4f_{5/2}$ at 161.71 eV and 166.9 eV energy, respectively, could be attributed to Bi^0 [48] in the g-C_3N_4/PVA@BiOCl photocatalyst. Two peaks in the Cl 2p spectrum (Figure 4c) at 200.22 eV and 202.46 eV were identified as Cl $2p_{3/2}$ and Cl $2p_{1/2}$, respectively [48,49]. in the high-resolution XPS spectra of C 1s that dipected in

Figure 4d, three peaks at 286.03 eV, 288.52 eV, and 290.52 eV may be deconvoluted into integrating sp^2 C–C bonds, sp^2-hybridized carbon (CN), and sp^3-coordinated carbon bonds from the g-C_3N_4 surfaces, respectively [50], the N 1s peaks at 399.24 eV, and 401.16 eV, as displayed in Figure 4e, were ascribed to sp^2-boned N that contributes in the triazine rings (CN=C) groups, and the tertiary nitrogen N–$(C)_3$, respectively [44,51,52]. In the O 1s XPS spectra displayed in Figure 4f, the lattice oxygen (O^{2-}) of Bi-O bounds, oxygen vacancy, and surface hydroxyl were identified as the three peaks at 532.86 eV, 534.94 eV, and 536.86 eV, respectively [53].

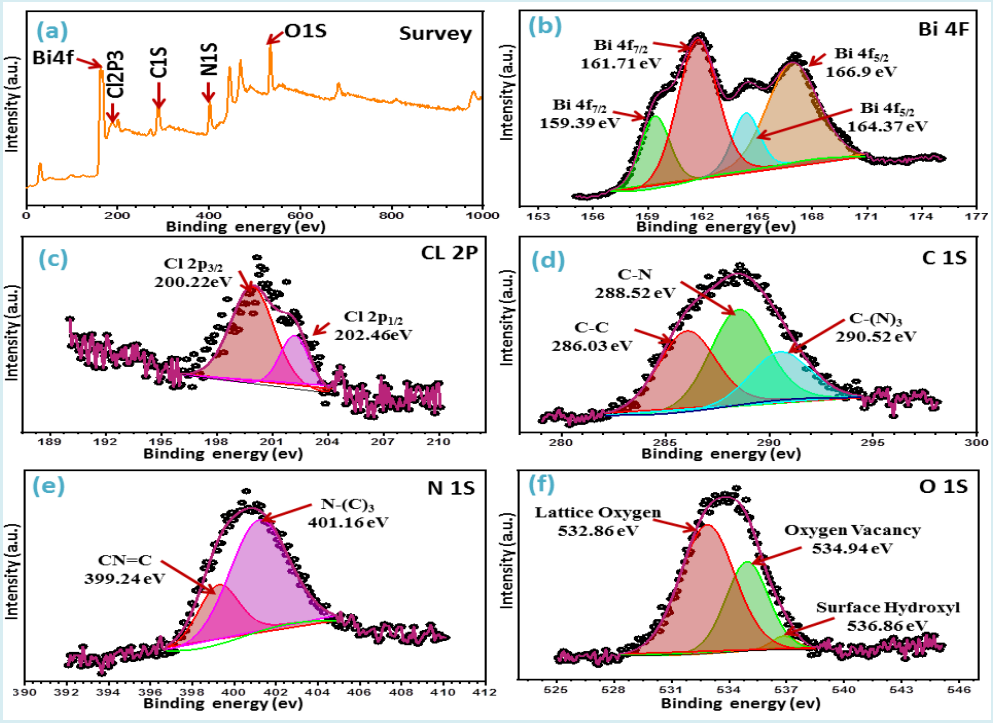

Figure 4: XPS spectra of g-C3N4/PVA@BiOCl photocatalyst: survey scan (a), Bi 4f (b), Cl 2P (c), C 1S (d), N 1S (e), and O 1S (f).

Optical Features

The optical feature is the primary factor influencing the sample's subsequent photocatalytic activity. Figure 5a displays the UV–vis diffuse reflectance spectra of pristine BiOCl, bare g-C_3N_4, and g-C_3N_4/PVA@BiOCl photocatalyst. The pristine BiOCl and bare g-C_3N_4 provide absorption bands at 370, and 490 nm, respectively. Furthermore, the g-C_3N_4/PVA@BiOCl absorption edge shifted to a higher wavelength, which indicates that composite photocatalyst may capture photons more efficiently than pure BiOCl in the area of visible illumination, resulting in increased valence electron excitation and the subsequent creation of additional active sites [43,49]. Illustration in Figure 5b was employed to estimate each photocatalyst's band gap energy, according to Kubellka-Munk theory, the optical absorption edge is found as follows [54]:

$$\alpha h\nu = A(h\nu - E_g)^n \quad (4)$$

A semiconductor's interband transition process determines the exponent n. For a direct inter-band transition, n equals 2, whereas for an indirect inter-band transition, it equals 1/2. g-C_3N_4 and BiOCl are both classified as indirect semiconductors with a value of n =½ [49,55]. The bare g-C_3N_4 and BiOCl exhibited band edge values of 2.7, and 3.3 eV, respectively. The band edge of g-C_3N_4/PVA@BiOCl is 2.5 eV red-shifted relative to that of the distinct pure parts. Which explained by the incorporation of g-C3N4 into BiOCl and their subsequent coupling. The findings demonstrate that in comparison to bare photocatalysts, g-C_3N_4/PVA@BiOCl photocatalyst is more capable of absorbing visible light [56,57]. The PL spectra of all samples with a λexcitation of 390 nm were displayed in Figure 5c. The g-C_3N_4/PVA@BiOCl composites' PL intensity was noticeably lower than those of the individual g-C_3N_4, and BiOCl, suggesting that photogenerated electron-hole recombination is suppressed and that the charge carriers are well segregated [47,58]. Therefore, it would be anticipated that the g-C_3N_4/BiOCl/CdS heterostructure photocatalyst would have a higher photodegradation performance than that of the pristine g-C_3N_4 and BiOCl.

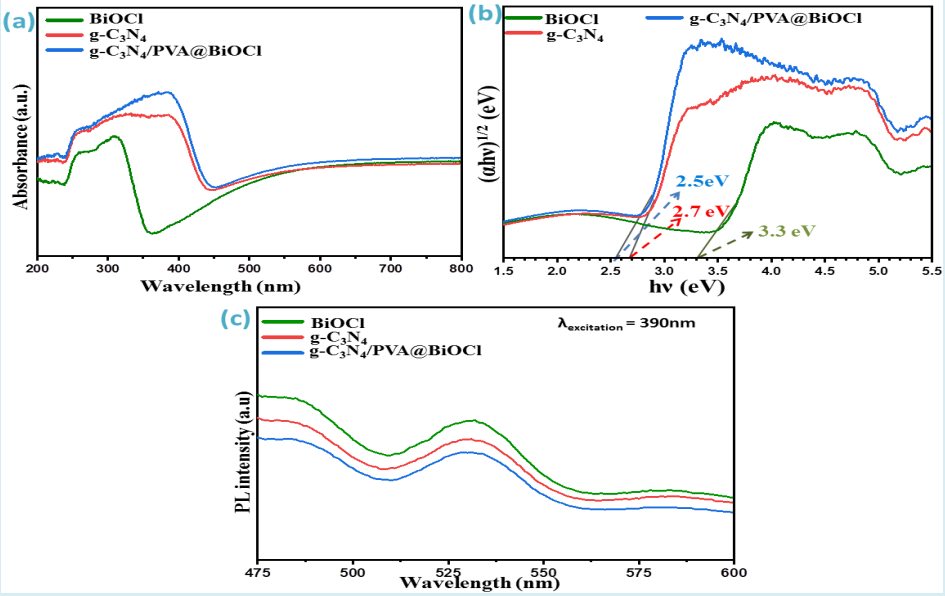

Figure 5: Diffused reflectance spectra (a); Tauc plot for determination of band gap (b) and PL spectra using λexcitation of 390 nm (c) of BiOCl, g-C3N4, and g-C_3N_4/PVA@BiOCl photocatalyst.

Photoelectrochemical Features

To assess the separating and transferring of the induced e^-/h_+ pairs on the exterior of produced photocatalysts, photoelectrochemical investigations are shown in Figure 6. Clearly, increased photocatalytic activity is caused by more effective electron and hole separation. Typical Nyquist plots of the synthesized photocatalysts are depicted in Figure 6a, for the g-C_3N_4 and g-C_3N_4/PVA@BiOCl a distinctive hemispherical arc is seen, implying that a single charge transfer mechanism is occurring among the working substance and electrolyte [59], also the Nyquist plots show a reduced arc radius for g-C_3N_4/PVA@BiOCl compared to individual g-C_3N_4 and BiOCl indicating a significantly lower impedance. This implies a lower interfacial layer resistance, which is advantageous for better separating and quicker interfacial transmission of e^-/h^+pairs.

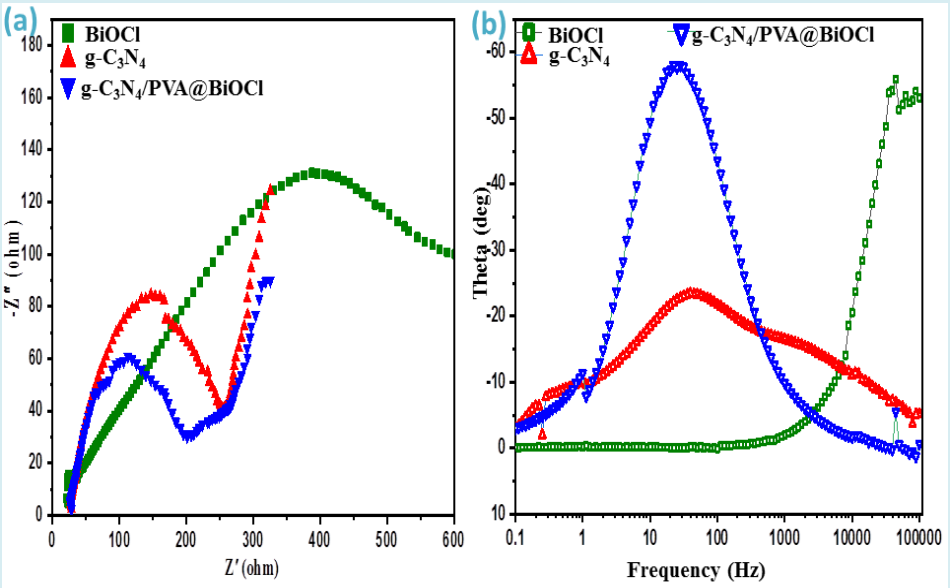

Figure 6: Photoelectrochemical features of the prepared photocatalysts: (a) EIS Nyquist spectra plots, and (b) EIS Bode spectra plots.

Figure 6b illustrates the Bode phase plot, which indicates the prevlent electrical activity of the system across a specific frequency range. The carrier lifetime (τ) data is shown in the Bode plot, and the carrier lifetimes were calculated at the maximum phase and observed frequencies [60,61].

$$t = \frac{1}{2}\pi F_{max} \quad (5)$$

where fmax is the maximum oscillation frequency of the impedance semicircle at the medium frequency region. g-C_3N_4/PVA@BiOCl shows less fmax than other samples, hence having a longer carrier lifetime (5.64ms). The results conclude that g-C_3N_4/PVA@BiOCl attained the maximal photocatalytic effectiveness concerning all prepared materials because of the prolonged carrier lifetime that results in a sluggish recombination probability.

Assessing the Photocatalytic Activity

Two different dyes (BB and OG) were used as module molecules with different molecular structures to investigate the photocatalytic effectiveness of BiOCl, g-C_3N_4, and g-C_3N_4/PVA@BiOCl under visible light as depicted in Figure 7 A separated mixture of dyes aqueous solution (BB and OG) with photocatalysts was exposed to stirring for 1h in darkness until reaching adsorption-desorption equilibrium. The mixtures were then subjected to treatment with visible light irradiation for 300 minutes.

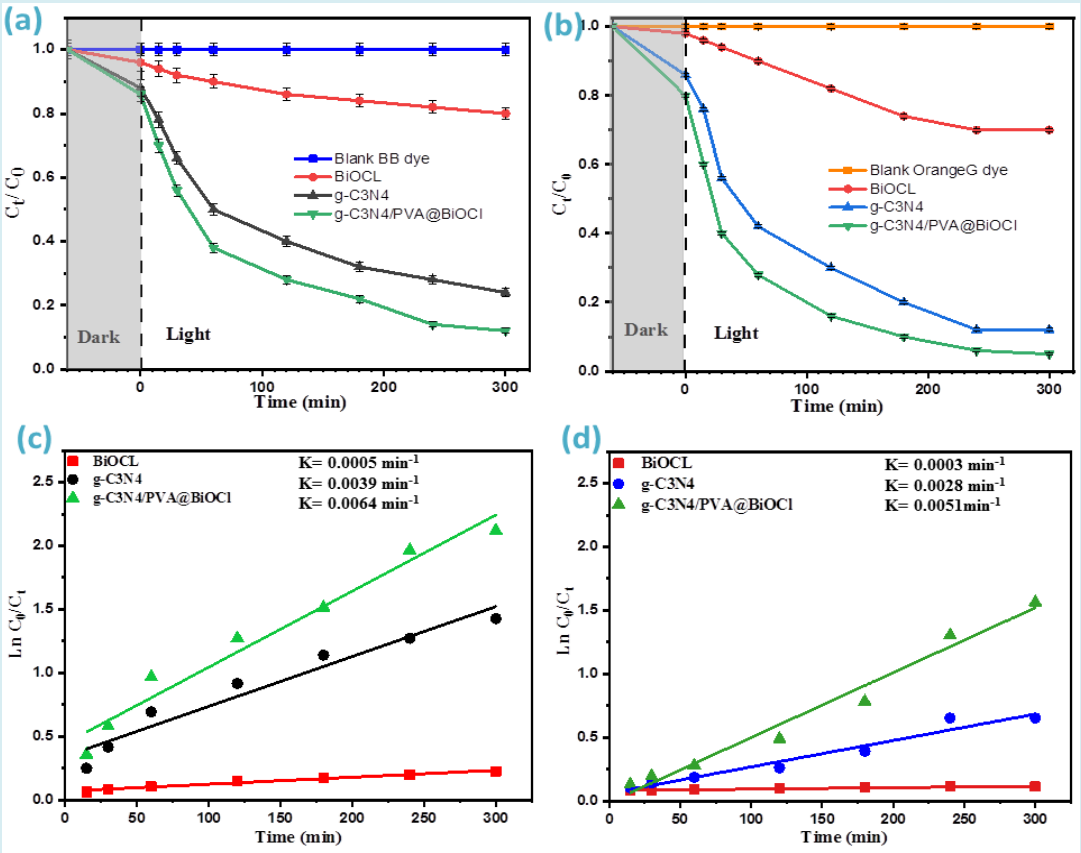

Figure 7: The photocatalytic degradation of (a) BB vs time, (b) OG vs time with different photocatalysts, (c) pseudo-first-order kinetic model of BB dye, and (d) pseudo-first-order kinetic model of OG dye degradation with prepared photocatalyst.

The UV-vis absorption spectra for all synthesized photocatalysts, as shown in Figure7a & 7b demonstrate that OG and BB deteriorated by raising illumination time. Furthermore, it ought to be noted that g-C_3N_4/PVA@BiOCl has a higher degradation rate than other samples (92.7%, and 81.9%) for OG and BB respectively. BiOCl and g-C_3N_4 deteriorated OG by 30%, and 88% respectively, and deteriorated BB by 20%, and 76% respectively.

BiOCl exhibited very poor dye degradation, while highly available adsorption sites in pristine g-C_3N_4, in addition to a reduction in the band gap energy value after a successful doping process of g-C_3N_4 in the BiOCl enhances the degrading efficiencies of g-C_3N_4/PVA@BiOCl.Also, the composite might serve as a trapping center, that successfully limits the recombination of photogenerated electron/hole pairs. As illustrated in Figure 7c & 7d the rate constant (k)

for all prepared photocatalysts was calculated by fitting the experimental data into a Langmuir-Hinshelwood pseudo-first-order kinetic model which is utilized to describe many photocatalytic reactions [62].

The g-C_3N_4/PVA@BiOCl photocatalyst had the largest kinetic rate constants (k) values of 0.0051 min-1 for OG dye and 0.0064 min-1 for BB dye. While rate constant values for pristine BiOCl and g-C_3N_4 were 0.0003 min-1 and 0.0028 min-1 for OG dye respectively and were 0.0005 min-1 and 0.0039 min-1 for BB dye respectively. In the g-C_3N_4/PVA@BiOCl, it was clear that recombination losses were greatly reduced and photocatalytic activity was improved. This also implies that the dopping of g-C_3N_4 might enhance charge separation, which would enhance the composite's ability to photodegrade.

A prior study found that the main factors that improved the efficiency of photocatalytic degradation were charge carrier lifespan, light absorption, and recombination rate [63]. Depending on the above results subsequent optimization analysis for the visible light photocatalytic degradation of OG dye and BB dye will be done with g-C_3N_4/PVA@BiOCl.

Factorial Design, Analysis of Variance Study (ANOVA), and Optimization Analysis

The central composite design, or CCD, is a strategy for multivariate designing including assessments of the appearance for several conditions that optimize degradation parameters and reduce the number of experiments that need to be conducted [64,65]. The impact of various degradation factors, (A) initial OG, and BB dye concentration mg/l, and (B) dose of g-C_3N_4/PVA@BiOCl g/l, on the deterioration efficiency of OG, and BB dye, has been examined in this study. Based on CCD the actual and predicted outcomes are presented in Table 1.

Run Order	A; Conc.of Dye mg/l	B;catalyst d=Dose g/l	Photo-Degradation % of BB		Photo-Degradation % of OG	
			Observed	Pridected	Observed	Pridected
1	150	1.27	79.3	77.88	78.1	75.59
2	100	0.25	69.8	68.84	72.5	75.62
3	150	0.425	63.5	63.62	65	66.63
4	100	0.85	80.2	81.13	81.8	81.98
5	100	1.75	89.4	90.2	89	91.52
6	100	0.85	80.6	81.13	81.8	81.98
7	50	0.425	81.9	82.46	92.7	88.32
8	10	0.85	98	97.99	100	99.5
9	50	1.27	92.8	94	98.5	97.28
10	200	0.85	62.7	63.13	61.3	60.29

Table 1: CCD for independent variables with experimental and predicted values for photo-degradation% of BB, and OG dye.

As suggested by the CCD model, an optimal degradation efficiency of OG, and BB at a time of 300 min, was reached 100% and 98% for actual response values, respectively at a preliminary dye concentration of 10mg/l, and catalyst dose of 0.85 mg/l. Also, the degradation efficiency of OG, and BB reached 98.5% and 92.8% for actual response values, respectively at a preliminary dye concentration of 50mg/l, and catalyst dose of 1.27 mg/l. The experimental study's outcomes can be modeled using the following quadratic model equation in terms of coded factors:

$$\text{Degradation efficiency}(\%)\text{ of OG dye}=+81.95-10.84A+4.48B \quad (6)$$

$$\text{Degradation efficiency}(\%)\text{of BB dye}=+79.56-8.79\,A+5.83B \quad (7)$$

Figure 8 illustrates the correlation between normal, anticipated, and real figures of the residual regarding the experimental data in the degrading execution of BB, and OG utilizing g-C_3N_4/PVA@BiOCl.

Figure 8a-8d represents normal % probability vs studentized residuals and predicted vs actual values for BB, and OG respectively, the scattering of data is depicted as a straight line in Figure 8c & 8d, indicating that the practical outputs were reliant upon the response's predicted values. Furthermore, residuals vs run number and residuals versus anticipated amount curves for the photo-degradation effectiveness of BB, and OG are shown in Figure 8e-8h, respectively. The residuals against the run number plot, as depicted in Figure 8e and 8f, exhibit a random dispersion

around zero with a change of ±4.38 and ±4.31 for BB, and OG respectively.

This result demonstrates that the model responses were typically distributed with the data [64]. The distinction between the studentized residuals and the predicted values has no individual form, as shown by Figure 8g and 8h. This supports the assertion that the proposed design is adequate and that the attained residuals exhibit the typical dispersal.

As shown in Figure 8i and 8j a lambda value of almost 1 in the Box-Cox plot for power changes, suggests that no modification is advised for the response of the BB, and OG's photo-degradation efficiency. As demonstrated in Figure 8k and 8l. Cook's distance measurements below 1 confirm that our model lacks effect points [66].

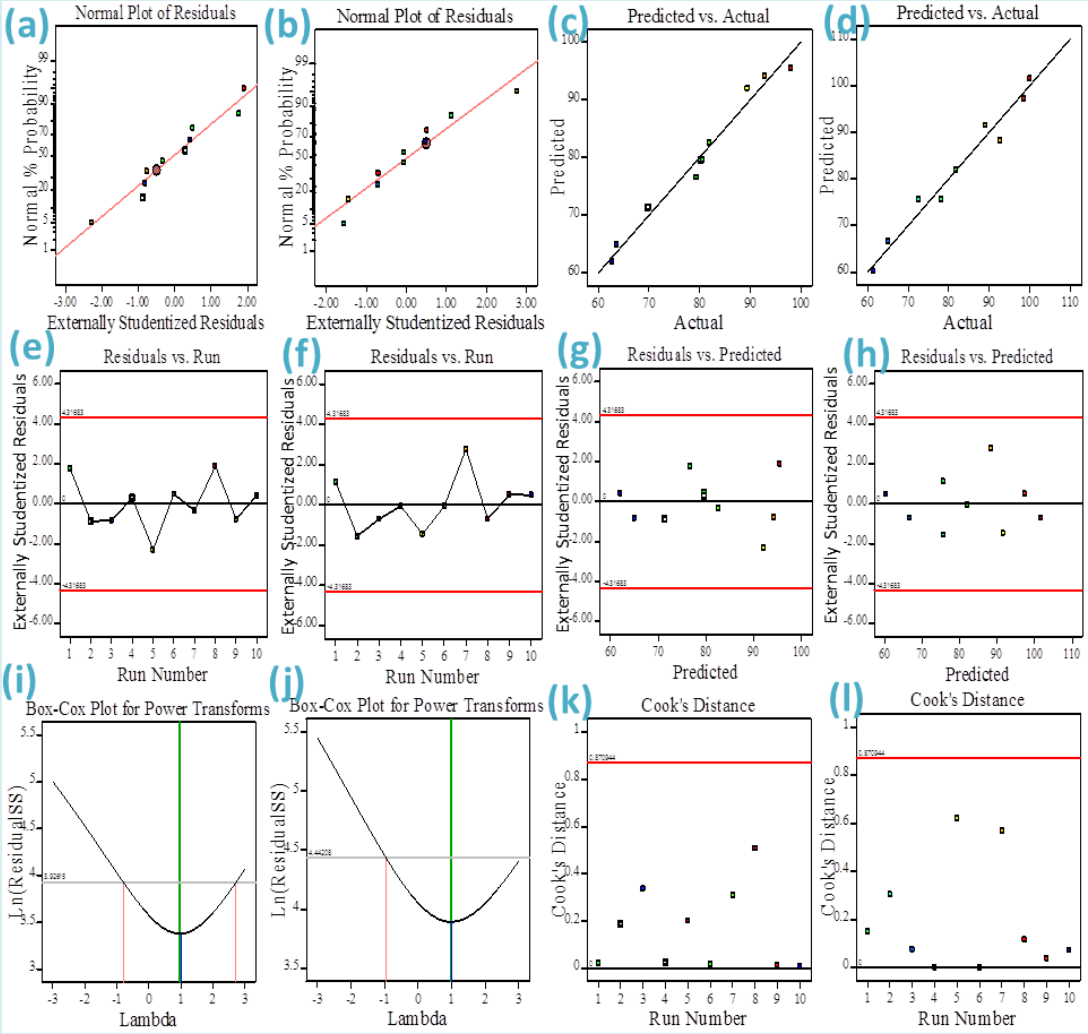

Figure 8 (a,b): Normal probability plot of the residual, (c,d) predicted versus actual amounts diagram, (e,f) residual versus run number, (g,h) residual versus predicated (i,j) a Box-Cox versus Lambda plot for the Power transformation, and (k,l) Cook's distance versus the run number for degrading of BB, and OG utilizing g-C_3N_4/PVA@BiOCl, respectively.

The goal of the ANOVA study was to manage both individual & combined influences of the variables on the photo-degradation execution of BB and OG. In the current investigation, the consequences of two distinct variations on the photo-degradation effectiveness of both dyes were explored with ANOVA, also, the findings of the ANOVA study are listed in Table 2. The excellence of the quadratic design integrated, including Fisher variation ratio (F-value), probability value (P value), Lack of Fit, and also the degrees of freedom (DF), the mean squares (MS), and the sum of squares (SS) were determined. The Model F-value of 146.53 and 109.38 for both BB and OG dyes demonstrates that the

model is significant; there is only a 0.01% chance that a model F-value" could occur due to noise. Probability values <0.0001 for the F-value denote that the model is significant. The findings showed that the terms A and B are significant for the degradation of both BB and OG dyes. In addition, system reduction may improve the system if there are insignificant model conditions (not including those necessary to maintain hierarchy) [66].

Dye	Source	SS	DF	MS	F value	P-value
	Model	1226.7	2	613.33	146.53	< 0.0001
	A-conc. of dye mg/l	868.48	1	868.48	207.49	< 0.0001
	B-catalyst dose g/l	356.77	1	356.77	85.23	< 0.0001
	Residual	29.3	7	4.19		
	Lack of Fit	29.22	6	4.87	60.88	
BB dye	Pure Error	0.08	1	0.08		
	Cor Total	1256	9			
	Model	1533.7	2	766.82	109.38	< 0.0001
	A-conc. of dye mg/l	1321.5	1	1321.5	188.49	< 0.0001
	B-catalyst dose g/l	210.84	1	210.84	30.07	< 0.0001
	Residual	49.07	7	7.01		
	Lack of Fit	49.07	6	8.18		
	Pure Error	0	1	0		
OG dye	**Cor Total**	1582.7	9			

Table 2: ANOVA analyses of a response surface for degradation of BB, and OG dye g-C_3N_4/PVA@BiOCl

In the current investigation, the 3D surface response plots and 2D contour plots are illustrated in Figures 9a-9d and displayed as visual illustrations of the correlation formula equation utilized to determine the optimum conditions of various conditions. These plots are typically utilized to attain a thorough comprehensive of the correlations among the different factors in the response. The results in Figure 9 demonstrate that the dual effects of initial dye concentration and photocatalyst dosage significantly affect the rate of BB and OG degradation.

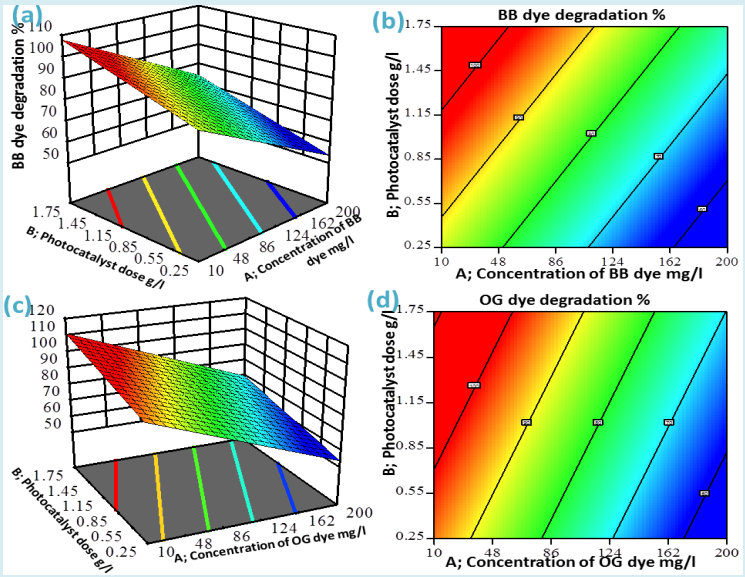

Figure 9: 3D-interaction effect plots of initial dye concentration and adsorbent doses (a,c), contour plots (b,d) for degradation of BB, and OG respectively, using g-C_3N_4/PVA@BiOCl.

Photocatalytic degradation efficiency was significantly improved by raising the photocatalytic dose starting from 0.25 to 1.75 g/L, with a deterioration rate reaching 98.5% and 92.8% of OG, and BB, respectively at a primary dye concentration of 50mg/l, and catalyst dose of 1.27 mg/l. While at a catalyst dosage of 0.25 g/L, the deterioration efficiency declined to 69.8% and 72.5% of OG, and BB dye, respectively at a primary dye concentration of 100mg/l.

The improvement of the accessible surface area of the photocatalyst and the production of more h+, •O2, and the MB pollutant could be mineralized and degraded by •OH radicals at the active regions., which can clarify why photocatalytic efficiency raised with the dose of the g-C_3N_4/PVA@BiOCl photocatalyst.

The interaction impact of dye concentration and the photocatalytic dosage on OG, and BB dye degradation results indicate that lowering the dye concentration and raising the photocatalyst dose value improved the photodegradation efficiency of both dyes. The degradation efficiency decreased from 98% to 62.7% for BB dye and from 100% to 61.3% with the rise in the initial dye concentration from 10 to 200 mg/L. Due to the photocatalyst being used having an acceptable surface area.

The degradation efficiency decreased at 200 mg/L of primary concentration because large amounts of oxidizing radicals such •OH and •O2 were needed to increase the oxidation process, and a decreased ability of deterioration was detected [67].

Trapping Experiment and Photocatalytic Mechanism

To verify the mechanism of the reaction on g-C_3N_4/PVA@BiOCl composite, the trapping study was employed. P-benzoquinone (PBQ), Ethylene diamine tetraacetic acid disodium salt (EDTA-2Na), and isopropanol (IPA) were employed to identify the active species including •O2−, h+and •OH, respectively. As shown in Figures 10a and 10b the photocatalytic activity was decreased with the addition of a BQ scavenger, implying that the superoxide radical •O2− was the primary reactive species.

The degradation effectiveness for both the OG and BB dyes decreased somewhat in the case of EDTA-2Na, suggesting that the photoinduced holes (h+) also had a significant influence on the photocatalytic activity.

The degradation performance moderately changed upon the inclusion of IPA, implying that the hydroxyl radicals (•OH) have a minor effect on the photocatalytic activity. To confirm and elucidate the type of active species involved in the photodegradation approach, the band positions of the produced photocatalysts were determined. Using the Mulliken electronegativity criteria, the band locations of CB and VB of the synthesized sample were found using the following equations;

$$ECB=X-Ee-0.5Eg \quad (8)$$

$$EVB = ECB + Eg \quad (9)$$

Where ECB is the potential of the conduction band, EVB is the potential of the valence band, X is the absolute electronegativity of the semiconductor, Ee is the energy of free electrons with a value of 4.5 eV, Eg is the band gap of the semiconductor [68], which is 2.7 eV for g-C3N4 and 3.3 eV for BiOCl. X is the absolute electronegativity, of g-C3N4 is 4.73 eV [69], and X of BiOCl is 6.36 eV [70]. The calculated ECB and EVB were −1.12 and 1.58 eV for g-C3N4, and 0.21 and 3.51 eV for BiOCl, respectively. Visible light can excite g-C3N4, which has a suitable bandgap. In the meantime, BiOCl may be photoexcited to produce e− and h+ since the fault degrees brought on by OVs can excite BiOCl with visible illumination.

The valence band (VB) potential of BiOCl and the conduction band (VB) potential of g-C3N4 allow for the generation of •OH/OH− (1.99 eV vs. NHE) and •O2− (O2/•O2−,−0.33 eV vs. NHE) [71]. Also, the boundary potential of g-C_3N_4's CB during the photo-reducing reaction of CO2 is lower than the typical redox potential of CO_2/CO (-0.53 eV) [72]. The possible distinction is adequate for the thermodynamic circumstances. The expected mechanism is depicted in Figure 10c.

The Z-scheme maintains the composite photocatalyst's better oxidation and reduction capabilities by combining the electrons on CB of BiOCl and the holes on VB of g-C3N4 while keeping the holes on VB of BiOCl and the electrons on CB of g-C_3N_4. Thus, the holes in the VB of BiOCl will further produce •OH radicals, while the electrons in the CB of g-C_3N_4 may give electrons to oxygen to make •O2− radicals. Specifically, BiOCl's surface OVs alter its electronic structure and create an entirely novel energy level that could allow photoelectrons to move to OVs [73].

Because of this, OVs act as e-traps and slow down e−, h+ pair recombination, increasing the lifespan of photoinduced carriers. Furthermore, at the 2D/2D interface, the g-C_3N_4/PVA@BiOCl heterojunction creates a powerful intrinsic electric field that facilitates the successful distinction of photogenerated electron-hole pairs. As a result, the created g-C_3N_4/PVA@BiOCl-OVs heterojunction with a 2D/2D structure has synergistic effects that can greatly enhance its efficiency of photocatalytic oxidation and reduction.

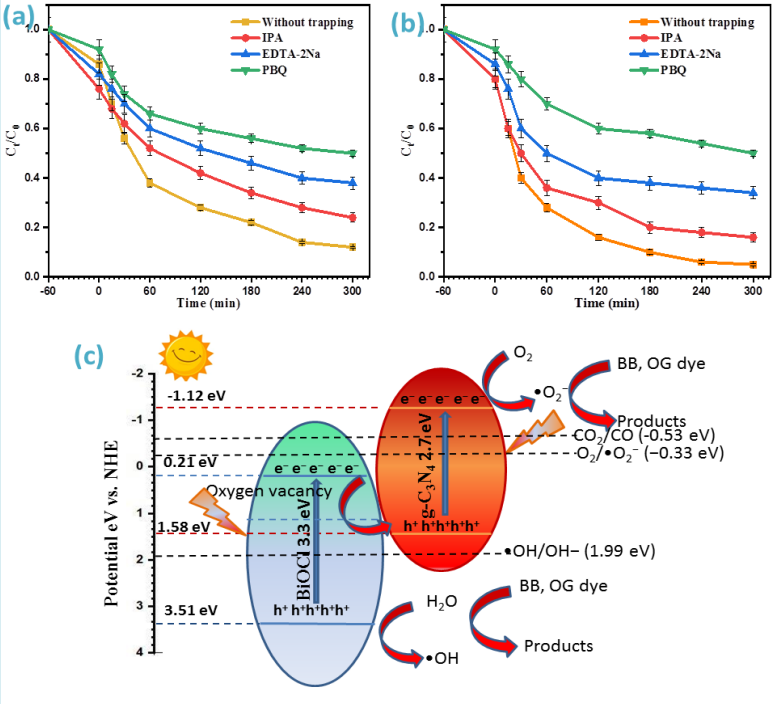

Figure 10: Trapping experiment for (a) BB dye, (b) OG dye, and (c) The possible photocatalytic reaction mechanism.

Catalyst Photostability

In the practical field, the durability and the renewability of the photocatalyst are important [74,75]. The synthesized g-C_3N_4/PVA@BiOCl underwent a recycling experiment under the mentioned identical reaction circumstance; herein the photocatalyst was collected after the deterioration of OG and washed with diluted HCL then distilled water. It was subsequently immersed into another 20 ml of 50 ppm OG dye solution. Figure 11 shows the photocatalytic efficiency of g-C_3N_4/PVA@BiOCl toward the deterioration of OG within four cycles. It may be found that the visible light photodegradation performance of OG reached 93%. These findings indicated that the g-C_3N_4/PVA@BiOCl showed superior durability and regeneration, making it a useful photocatalyst for real-world use.

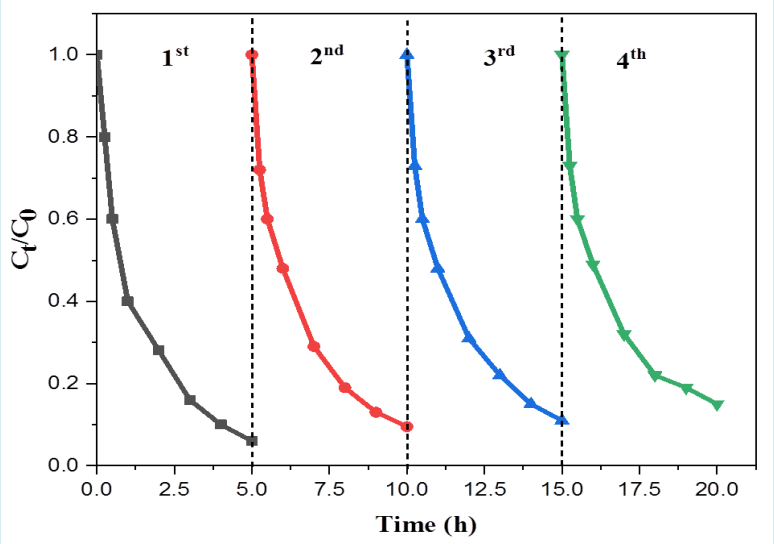

Figure 11: Recycled experiments for OG dye degradation over g-C_3N_4/PVA@BiOCl for four runs.

Conclusion

g-C_3N_4/PVA@BiOCl nanocomposite was synthesized with an environmentally friendly method. The inclusion of BiOCl nanoparticles and improvements of g-C_3N_4 with PVA were emphasized with (FTIR), (XRD),(TEM), (SEM–EDAX), (TGA), (XPS), and (PL). The inclusion of BiOCl and g-C_3N_4 is related to the improvement of the composite with oxygen vacancy. Results indicate that the prepared g-C_3N_4/PVA@ BiOCl novel 2D/2D composite deteriorates the BB and OG dyes through dual activities of adsorption/photodegradation. The response surface methodology (RSM) was used to statistically assess the influences of initial dye concentration and the photocatalyst dose on the degradation performance. Under optimum conditions of photocatalyst dose 0.85g/L, initial dye concentration of 10 ppm the degradation reached 100% and 98% for OG and BB dye respectively demonstrating its usefulness in visible illumination photocatalytic activity.

References

1. H Li, Zhang T, Tang X, Zhong J, Li J, et al. (2022) Effectively destruction of rhodamine B and perfluorooctanoic acid over BiOCl with boosted separation ability of carriers benefited from tunable oxygen vacancies. Colloids Surfaces A Physicochem. Eng Asp 649: 129470.

2. Cai W, Tang J, Shi Y, Wang H, Jiang X (2019) Improved in Situ Synthesis of Heterostructured 2D/2D BiOCl/g-C3N4 with Enhanced Dye Photodegradation under Visible-Light Illumination. ACS Omega 4: 22187–22196.

3. Li D, Xu K, Zhang C (2022) Improvement of Photocatalytic Performance by Building Multiple Heterojunction Structures of Anatase–Rutile/BiOI Composite Fibers. Nanomaterials 12.

4. Lei S, Fan J, Zhong J, Huang S, Li J (2021) Photoactivity of Bi 2 WO 6 synthesized by a solvothermal method using the different solvents. Appl Phys A Mater Sci Process 127.

5. Zhang P, Rao Y, Huang Y, Chen M, Huang T, et al. (2021) Transformation of amorphous Bi2O3 to crystal Bi2O2CO3 on Bi nanospheres surface for photocatalytic NOx oxidation: Intensified hot-electron transfer and reactive oxygen species generation. Chem Eng J 420: 129814.

6. Qin C, Lei S, Tang X, Zhong J, Li J, et al. (2020) Preparation of novel Ag/AgVO3/BiVO4 heterojunctions with significantly enhanced visible light-driven photocatalytic performance originated from Z-scheme separation of photogenerated charge pairs. Inorg Chem Commun 116: 107904.

7. Hu J, Fan W, Ye W, Huang C, Qiu X (2014) Insights into the photosensitivity activity of BiOCl under visible light irradiation. Appl Catal B Environ 158–159: 182–189.

8. Shang J, Chen T, Wang X, Sun L, Su Q (2018) Facile fabrication and enhanced photocatalytic performance: From BiOCl to element-doped BiOCl. Chem Phys Lett 706: 483–487.

9. Shi Y, Xiong X, Ding S, Liu X, Jiang Q, et al. (2018) In-situ topotactic synthesis and photocatalytic activity of plate-like BiOCl/2D networks Bi2S3 heterostructures. Appl Catal B Environ 220: 570-580.

10. Ouyang W, Teng F, Fang Z (2018) High Performance BiOCl Nanosheets/TiO2 Nanotube Arrays Heterojunction UV Photodetector: The Influences of Self-Induced Inner Electric Fields in the BiOCl Nanosheets. Adv Funct Mater 28(16): 1707178.

11. Hao L, Huang H, Guo Y, Du X, Zhang Y (2017) Bismuth oxychloride homogeneous phasejunction BiOCl/ Bi12O17Cl2 with unselectively efficient photocatalytic activity and mechanism insight. Appl Surf Sci 420: 303-312.

12. Dong H, Xiao M, Li J, HuW, Sun X, et al. (2020) Construction of H-TiO2/BiOCl heterojunction with improved photocatalytic activity under the visible and near-infrared light. J Photochem Photobiol A Chem 392: 112369.

13. Li X, Sun Y, Ren F, Bai Y, Cheng Z (2021) Smart oxygen vacancy engineering to enhance water oxidation efficiency by separating the different effects of bulk and surface vacancies. MaterToday Energy 19: 100619.

14. Zhao J, Li F, Wei H, Ai H, Gu L, et al. (2021) Superior performance of ZnCoOx/peroxymonosulfate system for organic pollutants removal by enhancing singlet oxygen generation: The effect of oxygen vacancies. Chem Eng J 409: 128150.

15. Ma X, Li W, Ren C, Li H, Liu X, et al. (20201) A novel noble-metal-free binary and ternary In2S3 photocatalyst with WC and "W-Mo auxiliary pairs" for highly-efficient visible-light hydrogen evolution. J Alloys Compd. 875: 160058.

16. Cai J, Cao A, Huang J, Jin W, Zhang J, et al. (2020) Understanding oxygen vacancies in disorder-engineered surface and subsurface of $CaTiO_3$ nanosheets on photocatalytic hydrogen evolution. Appl Catal. B Environ 267: 118378.

17. Wang J, Cao C, Zhang Y, Zhang Y, Zhu L (2021) Underneath mechanisms into the super effective degradation of

PFOA by BiOF nanosheets with tunable oxygen vacancies on exposed (101) facets. Appl. Catal. B Environ. 286: 119911.

18. Chen W, Xie J, Li X, Li L (2021) Oxygen vacancies and Lewis sites activating O3/H2O2 at wide pH range via surface electron transfer over CeOx@SiO_2 for nitrobenzene mineralization. J Hazard Mater 406: 124766.

19. Zeng K, Li W, Zhou Y, Sun Z, Lu C, et al. (2021) Multilayer hollow MnCo2O4 microsphere with oxygen vacancies as efficient electrocatalyst for oxygen evolution reaction. Chem Eng J 421: 127831.

20. Chen S, Huang D, Xu P, Xue W, Lei L, et al. (2021) Topological transformation of bismuth vanadate into bismuth oxychloride: Band-gap engineering of ultrathin nanosheets with oxygen vacancies for efficient molecular oxygen activation. Chem Eng J 420: 127573.

21. Chen X, Zhang X, Li YH, Qi MY, Li JY, et al. (2021) Transition metal doping BiOBr nanosheets with oxygen vacancy and exposed {102} facets for visible light nitrogen fixation. Appl Catal B Environ 281: 119516.

22. Chen J, Zhong J, Li J, Qiu K (2021) Boosted photocatalytic removal of tetracycline on S-scheme Bi12O17Cl2/α-Bi2O3 heterojunctions with rich oxygen vacancies. Appl Surf Sci 563: 150246.

23. Liu H, Fu H, Liu Y, Chen X, Yu K, et al. (2021) Synthesis, characterization and utilization of oxygen vacancy contained metal oxide semiconductors for energy and environmental catalysis. Chemosphere 272: 129534.

24. Sun Y, Wang H, Xing Q, Cui W, Wu S, et al. (2019) The pivotal effects of oxygen vacancy on Bi2MoO6: Promoted visible light photocatalytic activity and reaction mechanism. Chinese J Catal 40: 647-655.

25. Liu F, Liu X, Shen J, Bahi A, Zhang S, et al. (2020) The role of oxygen vacancies on Pt/NaInO2 catalyst in improving formaldehyde oxidation at ambient condition. Chem Eng J 395: 125131.

26. Bi X, Du G, Kalam A, Sun D, Yu Y, et al. (2021) Al-Sehemi, Tuning oxygen vacancy content in TiO2 nanoparticles to enhance the photocatalytic performance. Chem Eng Sci 234: 116440.

27. Liao H, Liu C, Zhong J, Li J (2022) Fabrication of BiOCl with adjustable oxygen vacancies and greatly elevated photocatalytic activity by using bamboo fiber surface embellishment. Colloids Surfaces A Physicochem Eng Asp 634: 127892.

28. Liu X, Wang H, Tu B, Wang W, Fu Z (2015) Novel divalent europium doped MgAlON transparent ceramic for shortwave ultraviolet erasable windows. Scr Mater 105: 30-33.

29. Rao F, Qin C, Zhong J, Li J (2021) Oxygen vacancies facilitated visible light photoactivity of CdWO4 prepared by ionic liquid assisted hydrothermal method. Ceram Int 47: 26572-26578.

30. Li H, Tang X, Zhong J, Li J, Chen G, et al. (2021) Carbon nanofibers induced tunable oxygen vacancies on BiOCl for high efficient destruction of decontaminants. Surfaces and Interfaces 25: 101247.

31. Khan MMR, Pal S, Hoque MM, Alam MR, Younus M, et al. (2019) Simple Fabrication of PVA-ZnS Composite Films with Superior Photocatalytic Performance: Enhanced Luminescence Property, Morphology, and Thermal Stability. ACS Omega 4: 6144-6153.

32. Cui D, Wang L, Xu K, Ren L, Weng L, et al. (2018) Band-gap engineering of BiOCl with oxygen vacancies for efficient photooxidation properties under visible-light irradiation. J Mater Chem A 6 : 2193-2199.

33. Zhang H, Tang G, Wan X, Xu J, Tang H (2020) High-efficiency all-solid-state Z-scheme Ag3PO4/g-C3N4/MoSe2 photocatalyst with boosted visible-light photocatalytic performance for antibiotic elimination. Appl Surf Sci 530:147234.

34. Zhang X, An D, Feng D, Liang F, Chen Z, et al. (2019) In situ surfactant-free synthesis of ultrathin BiOCl/g-C3N4 nanosheets for enhanced visible-light photodegradation of rhodamine B. Appl Surf Sci 476: 706-715.

35. Hong J, Hwang DK, Selvaraj R, Kim Y (2019) Facile synthesis of Br-doped g-C_3N_4 nanosheets via one-step exfoliation using ammonium bromide for photodegradation of oxytetracycline antibiotics. J Ind Eng. Chem 79: 473-481.

36. Majumdar A, Ghosh U, Pal A (2021) Novel 2D/2D g-C_3N_4/$Bi_4NbO8Cl$ nano-composite for enhanced photocatalytic degradation of oxytetracycline under visible LED light irradiation. J Colloid Interface Sci 584: 320-331.

37. Jingyu H, Ran Y, Zhaohui L, Yuanqiang S, Lingbo Q, et al. (2019) In-situ growth of ZnO globular on g-C3N4 to fabrication binary heterojunctions and their photocatalytic degradation activity on tetracyclines. Solid State Sci 92: 60-67.

38. Ding H, Liu Z, Zhang Q, He X, Feng Q, et al. (2022) Biomass porous carbon as the active site to enhance photodegradation of oxytetracycline on mesoporous

g-C_3N_4. RSC Adv 12: 1840–1849.

39. El-Sabban HA, Mady AH, Diab MA, Attia SY, Mohamed SG (2024) Construction of novel dual Z-scheme heterojunction of ternary CdS/g-C_3N_4/$NiFe_2O_4$ magnetically retrievable nanocomposite for boosted photocatalytic and energy storage applications. Surfaces and Interfaces 44: 103798.

40. Sun Y, Qi X, Li R, Xie Y, Tang Q, Ren B (2020) Hydrothermal synthesis of 2D/2D BiOCl/g-C_3N_4 Z-scheme: For TC degradation and antimicrobial activity evaluation. Opt Mater 108: 110170.

41. Zeng Z, Li K, Yuan T, Liang Y, Yang J, et al. (2021) Facile synthesis of BiOCl/g-C_3N_4 heterojunction via in situ hydrolysis of Bi nanospheres: a high-efficiency visible-light-driven photocatalyst. J Mater Sci Mater. Electron 32: 9972-9989.

42. Deng C, Hu H, Yu H, Xu JJ, Ci M, et al. (2021) Facile microwave-assisted fabrication of CdS/BiOCl nanostructures with enhanced visible-light-driven photocatalytic activity. J Mater Sci 56: 2994-3010.

43. Senasu T, Lorwanishpaisarn N, Hemavibool K, Nijpanich S, Chanlek N, et al. (2023) Construction of g-C_3N_4/BiOCl/CdS heterostructure photocatalyst for complete removal of oxytetracycline antibiotic in wastewater. Sep Purif Technol 306: 122735.

44. Zeng Z, Li K, Yuan T, Liang Y, Yang J, et al. (2021) Xiong, Facile synthesis of BiOCl/g-C3N4 heterojunction via in situ hydrolysis of Bi nanospheres: a high-efficiency visible-light-driven photocatalyst. J Mater Sci Mater Electron 32: 9972–9989.

45. Hou J, Wang H, Qin R, Zhang Q, Wu D, et al. (2024) Grinding preparation of 2D/2D g-C_3N_4/BiOCl with oxygen vacancy heterostructure for improved visible-light-driven photocatalysis. Carbon Res 3: 1–12.

46. Wang Q, Wang W, Zhong L, Liu D, Cao X, et al. (2018) Oxygen vacancy-rich 2D/2D BiOCl-g-C_3N_4 ultrathin heterostructure nanosheets for enhanced visible-light-driven photocatalytic activity in environmental remediation Appl Catal B Environ 220: 290–302.

47. Deng C, Hu H, Yu H, Xu JJ, Ci M, et al. (2021) Facile microwave-assisted fabrication of CdS/BiOCl nanostructures with enhanced visible-light-driven photocatalytic activity. J Mater Sci 56 : 2994–3010.

48. Cho WS, Hong DM, Dong WJ, Lee TH, Yoo CJ, et al. (2024) Porously Reduced 2-Dimensional $Bi_2O_2CO_3$ Petals for Strain-Mediated Electrochemical CO2 Reduction to HCOOH. Energy Environ Mater 7: e12490.

49. Cai W, Tang J, Shi Y, Wang H, Jiang X (2019) Improved in Situ Synthesis of Heterostructured 2D/2D BiOCl/g-C_3N_4 with Enhanced Dye Photodegradation under Visible-Light Illumination. ACS Omega 4 : 22187-22196.

50. Han N, Xu Q, Beyene G, Zhang Q (2020) Enhanced photocatalytic activity over g-C3N4/(BiO)2(OH)xCl2−x Z-scheme heterojunction. Appl Surf Sci 521: 146464.

51. Nie YC, Yu F, Wang LC, Xing QL, Liu X, et al. (2018) Photocatalytic degradation of organic pollutants coupled with simultaneous photocatalytic H_2 evolution over graphene quantum dots/Mn-N-TiO_2/g-C_3N_4 composite catalysts: Performance and mechanism. Appl Catal B Environ 227: 312-321.

52. Rohilla P, Pal B, Das RK (2023) Improved photocatalytic degradation of rhodamine B by g-C_3N_4 loaded $BiVO_4$ nanocomposites. Heliyon 9: e21900.

53. Durai M, Chauhan D, Durai M, Saravanan M, Kumaravel S, et al. (2022) Layered KTO/BiOCl nanostructures for the efficient visible light photocatalytic degradation of harmful dyes. Chemosphere 306: 135659.

54. Ali HR, Motawea EA (2021) Ternary Photodegradable Nanocomposite (BiOBr/ZnO/WO3) for the Degradation of Phenol Pollutants: Optimization and Experimental Design. ACS Omega 6: 22047-22064.

55. Deng C, Hu H, Yu H, Xu JJ, Ci M, Wu Y, Wang L, Zhu S (2021) Facile microwave-assisted fabrication of CdS/BiOCl nanostructures with enhanced visible-light-driven photocatalytic activity. J Mater Sci 56 : 2994-3010.

56. Tian G, Chen Y, Zhai R, Zhou J, Zhou W, et al. (203) Hierarchical flake-like Bi_2MoO_6/TiO_2 bilayer films for visible-light-induced self-cleaning applications. J Mater Chem A 1(23): 6961-6968.

57. Huo P, Li J, Ye Z, Wang H, Liu X, et al. (2017) Fabricated temperature sensitive photocatalyst of PNIPAM@ZnO/C for controllable photocatalytic activity. Chinese Chem Lett 28: 2259-2262.

58. Senasu T, Nijpanich S, Juabrum S, Chanlek N, Nanan S (2021)CdS/BiOBr heterojunction photocatalyst with high performance for solar-light-driven degradation of ciprofloxacin and norfloxacin antibiotics. Appl Surf Sci 567: 150850.

59. Banerjee R, Pal A, Ghosh D, Ghosh AB, Nandi M, et al. (2021) Improved photocurrent response, photostability and photocatalytic hydrogen generation ability of CdS nanoparticles in presence of mesoporous carbon. Mater

Res Bull 134: 111085.

60. Jung K, Lim T, Bae H, Ha HS, Morales AA (2019) Cu_2O Photocathode with Faster Charge Transfer by Fully Reacted Cu Seed Layer to Enhance Performance of Hydrogen Evolution in Solar Water Splitting Applications. ChemCatChem 11: 4377-4382.

61. Chen K, Feng X, Hu R, Li Y, Xie K, et al. (2013) Effect of Ag nanoparticle size on the photoelectrochemical properties of Ag decorated TiO_2 nanotube arrays. J Alloys Compd 554: 72–79.

62. Zargar SA, Gharivi M, Bagheri O, Khachatourian AM, Hashemi A (2024) Green synthesis of Z-scheme N-doped g-C_3N_4/Nd-doped ZnO heterostructure by pomegranate waste peel with enhanced photocatalytic performance for organic pollutants removal and antibacterial activity. FlatChem 48: 100736.

63. Solayman HM, Yahya NY, Leong KH, Hossain MK (2024) Photocatalytic performance of acid exfoliated graphitic carbon nitride (g-C_3N_4) for the degradation of dye under direct sunlight. FlatChem 48: 100762.

64. Ali HR, Motawea EA (2021) Ternary Photodegradable Nanocomposite (BiOBr/ZnO/WO_3) for the Degradation of Phenol Pollutants: Optimization and Experimental Design. ACS Omega 6: 22047-22064.

65. Motawea EA, Mubarak MF (2023) Optimisation and modeling of Organic Toxin elimination in waste water Based on Mesoporous GNS/NiO Nanocomposite. Int J Environ Anal Chem 103: 2445-2463.

66. Hasanpour M, Motahari S, Jing D, Hatami M (2021) Statistical analysis and optimization of photodegradation efficiency of methyl orange from aqueous solution using cellulose/zinc oxide hybrid aerogel by response surface methodology (RSM). Arab J Chem 14(11): 103401.

67. Lin W, Yu X, Zhu Y, Zhang Y (2018) Graphene Oxide/BiOCl Nanocomposite Films as Efficient Visible Light Photocatalysts. Front Chem 6.

68. Dang J, Guo J, Wang L, Guo F, Shi W, et al. (2022) Construction of Z-scheme Fe_3O_4/BiOCl/BiOI heterojunction with superior recyclability for improved photocatalytic activity towards tetracycline degradation. J Alloys Compd 893: 162251.

69. Wu C, Zuo H, Zhang S, Zhao S, Du H, et al. (2022) A Novel Strategy to Construct a Direct Z-Scheme Bi@$Bi_2O_2CO_3$/G-C_3n_4 Heterojunction Catalyst Via Pda Electronic Bridge. SSRN Electron J 294: 121242.

70. Zhang G, Liu Y, Zheng S, Sun (2021) Efficient removal of formaldehyde by diatomite decorated with BiOCl/TiO_2 under visible-light irradiation: Effects of key preparation parameters. Adv Powder Technol 32: 4364–4372.

71. Li S, Cai M, Liu Y, Wang C, Lv K, et al. (2022) S-Scheme photocatalyst TaON/Bi_2WO_6 nanofibers with oxygen vacancies for efficient abatement of antibiotics and Cr(VI): Intermediate eco-toxicity analysis and mechanistic insights. Chinese J Catal 43: 2652-2664.

72. Chen Y, Xu M, Wen J, Wan Y, Zhao Q, et al. (2021) Selective recovery of precious metals through photocatalysis. Nat Sustain 47(4) : 618-626.

73. Ji Z, Cai R, Ye W, Lu P, Dong CL, et al. (2023) Confined Fe single atomic sites on (100) plane of anatase TiO_2 nanofibers boost white LED driven Fenton-like norfloxacin degradation. J Clean Prod 382 : 135161.

74. Lin W, Yu X, Zhu Y, Zhang Y (2018) Graphene oxide/BiOCl nanocomposite films as efficient visible light photocatalysts. Front Chem 6: 385927.

75. Rajendran R, Varadharajan K, Jayaraman V, Singaram B, Jeyaram J (2018) Photocatalytic degradation of metronidazole and methylene blue by PVA-assisted Bi_2WO_6-CdS nanocomposite film under visible light irradiation. Appl Nanosci 8: 61-78.